Lawrence Berkeley National Laboratory

Lawrence Berkeley National Laboratory

Title

Measurements of Materials Shielding Properties with 1 GeV/nuc 56Fe

Permalink

https://escholarship.org/uc/item/6xh1d1pk

Authors

Zeitlin, Cary
Guetersloh, Stephen B.
Heilbronn, Lawrence H.
et al.

Publication Date

2006-05-15

Peer reviewed

eScholarship.org Powered by the California Digital Library
University of California

Measurements of Materials Shielding Properties with 1 GeV/nuc ^{56}Fe

C. Zeitlin*, S. B. Guetersloh, L. H. Heilbronn, J. Miller
Lawrence Berkeley National Laboratory, Berkeley, California 94720

Abstract. The design of future spacecraft such as the Crew Exploration Vehicle must take into account the radiation shielding properties of both the structural components as well as dedicated shielding materials. Since modest depths of shielding stop the vast majority of Solar Energetic Particles (SEP), the greater challenge is posed by the need to shield crew from the Galactic Cosmic Rays (GCR), which include highly-charged and highly-energetic particles. Here, we report on results from tests performed with beams of 1 GeV/nuc ^{56}Fe at the Brookhaven National Laboratory. A wide variety of targets, both elemental and composite, were placed in the particle beams, and the spectra of particles emerging from the targets were measured using a stack of silicon detectors. Results are presented primarily in terms of dose reduction per g cm^{-2} of target material, and support the conclusions of an earlier calculation by Wilson *et al*. showing that performance improves as the shield's mass number decreases, with hydrogen being by far the most effective. The data also show that, as depth increases, the incremental benefit of adding shielding decreases, particularly for aluminum and other elements with higher atomic mass numbers.

Key words: space radiation, Galactic Cosmic Rays, shielding, heavy ions, fragmentation, radiation dose, dose equivalent
PACS: 25.75-q, 98.70.Sa

1. Introduction

Increases in the duration of crewed space missions, and the likelihood of missions outside Low-Earth Orbit (LEO), are driving the need for a deeper understanding of the health effects of space radiation so that the risks to personnel can be better managed [1]. The National Aeronautics and Space Administration has established a program devoted to exploring radiation-induced health hazards that humans may encounter in deep space travel. Taking a systematic approach to the reduction of the known risks to crew health, safety, and performance during and after long-duration space flight, NASA has developed the Bioastronautics Critical Path Roadmap [2]. The use of shielding materials is one of the specific countermeasures listed in the roadmap, but the choice of which particular material or materials to use remains undefined. Here, we report on a series of measurements made using a particle beam, 1 GeV/nuc ^{56}Fe, that is representative of the

* Corresponding author. Email: cjzeitlin@lbl.gov, Fax: (510)486-6949

heavy ion component of the Galactic Cosmic Rays (GCR), and a variety of shielding materials including composites, light elements, and heavy elements.

Highly energetic Galactic Cosmic Rays can penetrate many g cm^{-2} of matter; e.g., the 1 GeV/nuc ^{56}Fe ions used in this work have a range of 12.6 cm, or 34 g cm^{-2}, of aluminum. Exposure to such particles and their nuclear interaction products is unavoidable on deep-space missions. Because of the extreme constraints on payload mass and the high energies of many GCR particles, reducing the risk in flight by the use of very massive shielding is not an option. Instead, it will be necessary to find materials that efficiently reduce risk without adding excessive mass to the spacecraft.

Although there are, at present, no defined career exposure limits for astronauts on long-duration spaceflights, we can take the established limits for LEO [1] as a starting point. The maximum allowable exposures are those that – factoring in the considerable uncertainties in biological response – increase an individual's lifetime fatal cancer risk by 3%. As the increase in lifetime risk depends on both the astronaut's age and gender at the time of exposure, the limits are determined on a case-by-case basis. In the present paradigm, dose equivalent is used as the physical quantity that relates to cancer risk. Career dose equivalent limits vary from 0.5 Sv for younger females to 4 Sv for older males. On a Mars mission undertaken near solar minimum, when the GCR are at their maximum flux, a 1000-day mission would, with minimally effective shielding, result in an accumulated GCR dose equivalent on the order of 1 Sv [3]. By itself, this is above the LEO career limit for some astronauts, and any Solar Particle Events occurring over the course of the mission would add to the accumulated dose equivalent. Therefore, unless a decision is made to relax the criteria for acceptable radiation exposures in deep-space missions, or effective biological countermeasures are discovered, shielding will play a crucial role in enabling these missions.

As high-energy, highly-charged particles (referred to as HZE particles) traverse a target, e.g., tissue or the hull of the spacecraft, they undergo electromagnetic and nuclear interactions. These two types of interactions – but particularly the nuclear – result in

fragmentation of the incident ions into lighter charged particles and neutrons. In many reactions, the fragments are of less biological significance than the incident ion. Thus fragmentation of the incident heavy ions may be an important mechanism for reducing the risks associated with exposure to the GCR. For incident ions with very high LET (above the peak of the quality factor curve), fragmentation may produce a lighter ion with a higher quality factor, thus producing a particle that delivers a lower dose but a higher dose equivalent than would have been the case if not for the fragmentation event. More typically, though, fragmentation produces secondary particles that deliver a smaller dose and dose equivalent than the incident particle would have.

The other important mechanism in the transport of energetic heavy ions through matter is ionization energy loss. Some of the kinetic energy of the incident particle is transferred to the electrons of the medium being traversed, reducing the velocity of the ion as it penetrates deeper into the material. The linear energy transfer in water (LET[1]) of a given ion, and hence the dose it delivers, increases with depth since dE/dx depends to first order on the inverse square of velocity. Ions with sufficient range to fully traverse the shielding emerge with higher LET and may be more biologically damaging than the incident ion would have been had there been less material in its path. On the other hand, lower-energy ions (more typical of SPE than the GCR) can be stopped by modest depths of shielding. Thus, depending on the energy spectrum of the incident particles, the effects of energy loss can be either helpful or harmful in terms of total dose or dose equivalent behind shielding.

Given the mix of particle types and energies impinging on a spacecraft, the risk presented by the complex modified field in the inhabited areas will be strongly influenced by both fragmentation and energy loss, and will depend on the details of the incident particle flux and the composition of the shielding materials. In heavily shielded locations, such as a lunar or planetary habitat buried deep underground, secondary neutrons may contribute substantially to the dose equivalent [4]. In the laboratory environment, we expect neutrons to make important contributions when very thick targets are used (thick enough

[1] We use LET as shorthand for LET_{∞} , i.e., the energy deposited in an infinite volume of water.

to stop the primary beam ions) and/or when beam energies are substantially lower than in the experiments reported here. In this work, we focus on secondary charged particles, which dominate the dose and dose equivalent at modest shielding depths.

Although the full space radiation environment cannot be reproduced in the laboratory, we can study individual ions at specific energies and compare those results to predictions from the transport models such as HZETRN [5] used by NASA for risk assessment. Some combinations of ion species and energy may be more relevant for this purpose than others. According to radiation environment model calculations for free space, the ion species that makes the largest contribution to dose equivalent is iron, and near the maximum of the solar cycle, roughly half of the flux of iron is at energies of 1 GeV/nuc and above. For this reason, 1 GeV/nuc ^{56}Fe was selected for use in most of the radiation biology runs sponsored by NASA at the Brookhaven National Laboratory's Alternating Gradient Synchrotron (AGS) from 1995 to 2002, and also at the NASA Space Radiation Laboratory (NSRL) in more recent runs. During each run, beam time was made available for physics studies, which largely focused on cross section measurements [6], beam characterization [7], and shielding studies such as the present work and the study described in the accompanying paper [8]. All measurements made by our group were performed using a stack of silicon detectors, applying analysis methods described in the aforementioned references. Here, we present a simple data analysis technique that allows us to study the change in dose per incident particle when the beam passes through a variety of target materials and depths. The analysis applies to all targets, regardless of whether they are elemental or composite. The spectra used to compute dose per incident particle could also be used to compute dose equivalent per particle; however, in the interests of keeping to purely physical quantities that are simply related to the measured quantities, we use dose per incident beam particle. Dose equivalent measurements with polyethylene targets are discussed in [8].

To determine the amount by which the dose at the target exit is changed relative to the dose delivered by an incident iron particle, we make use of (1) the approximation that the deposited energy (ΔE) in a silicon detector is proportional to LET spectra in water, and

(2) the fact that the total dose imparted by a mixed radiation field is proportional to the average LET[2] of the entire distribution. The average LET of the mixed field, divided by the LET of the incident ^{56}Fe, is a measure of the change in dose due to the target. It is also of interest to examine the change in dose divided by the areal density of the target (i.e., its depth in g cm^{-2}), so that targets of different areal densities can easily be compared on the same scale. For several target materials, we have enough data to study these quantities as functions of depth over a considerable range, and we can extrapolate those results to zero depth, putting all materials on an equal footing for purposes of comparison.

Much of the motivation for this work is due to the earlier work of Wilson et al. [9, 10] in which the authors used their GCR transport model to show that hydrogen, and hydrogenous materials such as methane, should be the most effective shields for long-duration deep space missions. No particle accelerator can reproduce the complexity of the GCR, and in any case practical considerations such as the availability of beam time dictated that most of these tests be performed with a single beam ion and energy. Therefore we cannot claim to have directly tested Wilson's predictions. However, in the accompanying paper [8], we show that 1 GeV/nuc iron provides a reasonable proxy for the heavy ions in the GCR, and that our results are – at least qualitatively – in excellent agreement both with the predictions of Wilson et al. and with the predictions of our own Monte Carlo simulation.

2. Materials and Methods

Most of the data presented here were taken at the AGS from 1995 to 2002. Additional data were taken at the NSRL in 2004. All measurements were performed with silicon detectors in various configurations. Though the details of the configurations varied, the general principle was the same in each: particles emerging from the vacuum exit window were incident on one or more silicon detectors placed upstream of the target that were

[2] We refer to "event-averaged" LET, an approximation to track-averaged LET (defined below).

used to trigger the readout; particles next entered the target, and those emerging from the target were measured in two or three sets of detectors placed along the beam axis at different distances from the target exit. Trigger thresholds in the upstream detectors were typically set so that only an incident iron ion produced a trigger. Among the downstream detectors, the first set always subtended a relatively large part of the forward cone defined relative to the target center along the nominal beam centerline. We characterize the forward cone by its half-angle; a 5º to 10º acceptance angle was typical for the first downstream detectors, referred to as the "large-acceptance" detectors. Schematic diagrams of our experimental setups have been published earlier [6, 7], and also in the companion article to this one [8].

A calculation of the acceptance efficiency was performed using the Goldhaber model [11] of transverse momentum transfer in nucleon-nucleon collisions. Results indicate that, for a 1 GeV/nuc ^{56}Fe beam, virtually all of the "heavy" fragments (defined as having charge 10 or greater, for an iron beam at this energy) are within the cone subtended by our large-acceptance detectors. Other detectors were placed further downstream from the taget position, with typical acceptance angles of 1º to 2º; these detectors were traversed by fewer fragments owing to the smaller angles subtended. The effect of different acceptance angles is illustrated in Figure 1, in which typical charge spectra are shown. At large acceptance (Fig. 1a), fragment peaks are visible down to charge 10, while at small-acceptance (Fig. 1b) clear peaks are visible for all fragment charges. The difference is due to events in which there were only light fragments; in those cases, the large-acceptance detectors are typically hit by multiple fragments in coincidence, and the large number of possible detected combinations causes the peaks to wash out. The small acceptance detectors see a lower multiplicity, reducing the number of possible multiple-fragment combinations; the resulting spectra show single-fragment peaks that are relatively free of distortion.

In the data taken prior to 2002, the beam energy as determined by ΔE in silicon and separately by Bragg curve measurements using a variable-depth water column and ionization chambers was consistently found to be 1064 MeV/nuc at the exit of the

vacuum window on the beam transport line. In 2002, the energy was about 990 MeV/nuc at the same point. At the NSRL, the beam energy at the exit window was 998 MeV/nuc. These small variations have no discernible effects on the results, as determined by measurements made with the same targets at all three beam energies.

3. Data Analysis

a. Event Selection

Both this analysis and cross section analysis require us to obtain the ΔE spectrum behind each target. The methods used to obtain clean ΔE spectra for this analysis are the same as described in detail in references [6] and [7]. In the first step of the off-line data analysis, the digitized pulse heights recorded during the runs are converted to ΔE for each detector. This requires the use of calibration data, obtained in dedicated short data-taking runs, in which a digital-to-analog converter (DAC) under computer control steps through a series of voltages which are applied to each preamp circuit's calibration capacitor. Charge is injected into the preamplifier as if it were coming from the detector; the charge injected Q_{inj} is given simply by $Q_{inj} = C_{cal} \times V_{dac}$ where C_{cal} is the value of the calibration capacitor and V_{dac} is the applied voltage. Charge collected is related to ΔE in silicon assuming that one electron-hole pair is produced for each 3.6 eV deposited. The absolute ΔE scale is not critical in the final results, for reasons explained below; when compared to detailed calculations of deposited energies in the detectors, an accuracy of better than ± 5% is obtained, with the error dominated by the uncertainty in the value of the calibration capacitors.

Once the data have been converted to ΔE, we make cuts on the spectra of the detectors upstream of the target to select only events in which a single Fe ion entered the target. Next, a scatter plot of the ΔE in each of the first two downstream detectors is made. Graphical cuts are made in this plot to select events along the 45º line, i.e., events in which the two detectors gave a mutually consistent ΔE. This cut removes events in which the particle underwent a charge-changing interaction in either detector and also those in

which one detector or the other gave a spurious reading[3]. For events passing the cuts, a histogram of ΔE summed in the two detectors is made, and this can be used to create a second histogram of charge, Z, as in Fig. 1. The absolute scale of ΔE is subject to uncertainty from the variations in the individual calibration capacitor values, detector dead layers, and, in those cases where position-sensitive detectors are used for the analysis, less than 100% charge collection efficiency. To work around these issues, we use the primary iron peaks found in target-out data to provide a point of known LET, i.e., to determine a constant of proportionality for each detector's ΔE to LET. The constants are then used in the analysis of the target-in runs. This procedure essentially eliminates possible errors in the ΔE scales determined by pulser calibration. Calculations show that the approximation $\Delta E \propto LET$ is good to about ± 1% for the energy range relevant to these measurements, from about 400 MeV/nuc to 1 GeV/nuc.

b. Analysis Method Based on ΔE Distributions

Two analysis methods were used initially, one comparatively simple and the other more elaborate. In the simpler analysis, the average ΔE's are used to estimate the shielding-induced change in the dose per particle, δD, according to

$$\delta D = (1 - LET_{avg\text{-}in}/LET_{avg\text{-}out}) = (1 - \Delta E_{avg\text{-}in} / \Delta E_{avg\text{-}out}) \quad \text{[equation 1]}$$

where the subscripts refer to the presence (in) or absence (out) of a target. (We will explain what we mean by "average" below – in the context of this experiment, it is not a simple track average.) Both the average ΔE values and the δD results are of interest; for a given material, a plot of average $\Delta E_{avg\text{-}in}/\Delta E_{avg\text{-}out}$ vs. target depth is essentially a Bragg curve, and the first derivative of this quantity (or, equivalently, of δD) vs. depth shows the efficacy of an additional increment of shielding as a function of depth.

Since targets of many depths were used in this study, it is desirable to display the results in a manner that is independent of depth, if possible. The simplest approach is to simply divide out the depth of the sample used. This yields a quantity we refer to as δD_n, the

[3] Most mismeasured events occur when a particle's trajectory causes it to hit the detector near its outer edge, where the silicon is not fully depleted due to distortion of the internal electric field.

normalized dose reduction, with units of $(g\ cm^{-2})^{-1}$. A second approach, used when we have data for a given material at two or more depths, is to fit a simple exponential to δD_n vs. depth and extrapolate the curve to zero depth.

The method of using average ΔE to determine δD and δD_n introduces a small systematic bias in the spectra, which is due to nuclear interactions in the detectors downstream of the target. The probability of a nuclear interaction in the detector (and therefore removal of the event in the analysis) depends on the mass of the particle traversing the detector, so that the correlation cut made to select the sample preferentially removes more events with iron or high-Z fragments than it does events with light fragments. This is a small effect, particularly when the thin position-sensitive detectors (approximately 1 mm each in depth) are used. It is this bias that the second analysis method, described below, was explicitly designed to remove.

Equation 1 contains implicit compensation for fragments formed in beamline materials other than the targets, in that the average LET of the target-out data is used, rather than simply the LET of the primary. Though small, this compensation is needed because primary ions fragment into lighter ions with lower LET as they traverse air gaps, entrance and exit windows, and detector dead layers. Such events appear as well-measured fragments in the spectra, but they are artifacts in the sense that they are not produced in the target, and therefore their contribution to δD_n must be accounted for.

c. Definition of Average LET

In a mixed radiation field, dose and dose equivalent are defined in terms of LET distributions. In a fragmentation event, the incident nucleus is broken up into at least two pieces. With projectile velocities in the relativistic range ($v/c \approx 0.88$ in these experiments), the fragments have angular distributions that are sharply peaked in the forward direction. This means that fragmentation events frequently result in the presence of multiple particles being recorded, especially in the detectors closes to the target exit. It is therefore not possible to calculate a true track-averaged LET with these data. Instead, we define an "event-averaged" LET that assumes a multiplicity of 1 particle for every

event, even when fragmentation has occurred. When a primary passes through the target without interacting – as is the case in the vast majority of events when thin targets are used – this is formally correct; and when a fragmentation event is peripheral, as most of them are, and the projectile undergoes a relatively small charge change, the leading fragment (heaviest and typically most forward-going) dominates the dose. In those cases, the event-averaged LET can be considered as the leading-fragment LET to a good approximation. The event-averaged LET is directly related to the total dose behind the target per incident beam ion. This is still not the same as track-averaged LET, however. When central collisions occur and produce a high multiplicity of ions much lighter than the primary, the meaning of the event-averaged LET is less obvious. We return to this point and its implications below.

d. Alternate Analysis Method Using Z Distributions

The second method of determining the dose reduction explicitly addresses the issues of background fragments and events lost in the detector stack. It has the disadvantage of imposing the approximation that fragments on average emerge from the target at the same velocity as the surviving primary iron ions. In reality, fragments lose less of their velocity in traversing the target from their production point forward, and so on average they emerge at slightly higher velocities than the primaries. This approach therefore results in a small systematic bias towards higher assigned LET, and lower dose reduction, than is actually the case. The degree of bias introduced depends on the target thickness, with the effect growing in importance as target depth increases.

To perform the second analysis, we use the histograms of Z and count the number of events for each species from iron to neon ($Z = 10$). Events with $Z < 10$ are grouped in a single category and assigned an average LET determined from the average ΔE of the events. The number of ions of each species is corrected by dividing by the calculated probability[4] that an ion of that species traverses the silicon detectors without undergoing a charge-changing interaction. The target-out data are used to produce a similar

[4] The calculation is based on geometric cross sections and assumes masses that correspond to the most abundant naturally-occurring isotope of each species.

histogram of the number of events per species, and those counts are also corrected for losses in the silicon. The corrected target-in counts as a function of Z are then further corrected by subtraction of the background fragments as determined by the target-out data. Both corrections have the effect of increasing the relative numbers of primaries and reducing the relative numbers of fragments, thus increasing ΔE_{avg}. The result of these manipulations is a histogram of charge, Z, which is converted into a coarsely-binned histogram of LET by assuming $L = k Z^2$ where k is a constant determined from the location of the iron peak in the ΔE histogram, relative to its location in the ΔE target-out histogram. A simple average LET of this distribution is then determined and used to determine dose reduction as per equation 1. As in the analysis method described above, this is an "event-averaged" LET value, i.e., no attempt is made to account for multiplicities greater than one.

e. High-multiplicity Events and Small Acceptance Spectra

As mentioned above, a significant complication arises from central collisions – events in which no high-charge fragment is present because the incoming iron nucleus is mostly or entirely broken apart. These events appear in the large-acceptance detector spectra in the region of the plot with no distinct peaks. Using the event-averaged LET treats the full recorded ΔE on such an event as if it were due to a single particle, when in fact it was the sum of multiple lighter ions. Since the detectors register most or all of the particles in the forward cone, LET is overestimated on these event; the event-averaged LET is therefore also overestimated. This yields a lower measured value of δD than would be seen by a small-area detector, or a biological sample. The magnitude of the effect depends on the target depth and type, as it is governed by the probability of a central collision occurring. When there is a high multiplicity of light fragments, and no heavy fragments, the small-acceptance detectors are hit by a low multiplicity of only the most forward-produced fragments, and – as in the case of the large-acceptance detectors on events with heavy fragments – the recorded ΔE corresponds to that of the most forward-going fragment. This is certainly more easily interpreted than the large-acceptance ΔE recorded on such events.

To understand the effect of these events on the results, we undertook a study of the low end of the LET spectra for several targets, and the effect of this region on the overall results. Using small-acceptance detectors to determine dose reduction gives values that are, for the great majority of targets, about 10 to 15% larger than the values obtained with large-acceptance detectors; this goes in the expected direction. (It is important to note that the differences seen here are highly dependent on the acceptance angle of the small-acceptance detectors.) For Cu and especially Pb targets, we saw larger differences between large- and small-acceptance spectra. This is because Coulomb interactions in high-Z materials cause many primary beam ions to scatter out of the downstream detector's acceptance. Events in which a primary scatters out are removed in the data analysis, whereas fragmentation events are kept even if the leading fragment scattered out. This biases the ΔE distributions in these cases and results in a larger apparent δD than is seen in the large-acceptance detectors, where the scattering-out losses are negligible. Therefore to avoid biasing our results, all data presented here are based on spectra obtained with large-acceptance detectors, despite the fact that the small-acceptance detectors record spectra that are more directly comparable to the particle fluence a cell would see.

f. Comparison Between Analysis Methods

As expected, the results given by the two data analysis methods (ΔE_{avg} or Z histogram) are similar. The dose reductions found by the two methods were typically within 4% of one another, with the largest difference found to be 15%. In Fig. 2, we show a scatter plot of δD_n values obtained by the two methods for a subset of the data. There is a small shift to lower δD using the Z-histogram method; those values are usually smaller than the δD values found by the ΔE method. As explained above, the discrepancies between the two methods are expected to be dependent on target depth, so we cannot use this subset to make a general statement about the systematic differences. For the work shown here, the ΔE method was used.

g. Uncertainties

Statistical errors are negligible in this analysis since the data samples all contain a minimum of several tens of thousands of events. The main source of uncertainty in these measurements is systematic, related to the analysis method used to define the event samples. These samples are defined by drawing graphical cut contours in scatter plots of ΔE recorded in adjacent detectors. The cuts are made as consistently as possible, but there is inevitably some ambiguity about whether to include or exclude certain events. In particular, in a typical scatter plot (see, e.g., Fig. 2 of Ref. [12]), there is a dense cluster of data points due to the primary ion. In most cases, there are noticeable tails to the low end of the ΔE distribution in one or both detectors; there can also be tails to the high end. Some of the events in the tails may be due to nuclear interactions in the silicon detectors, some may conceivably be due to less than 100% charge collection, and others are simply due to the finite resolution of the detectors and electronics. In making the graphical cuts, we are attempting to remove events in which an interaction occurred in either detector, but a peripheral reaction near the exit of the second detector of the pair, in which just one or two charge units are lost, may well result in a ΔE that puts the event in the tail of the primary distribution. The challenge in the analysis is determining how tight to make the cut, and to draw contours that yield equal efficiencies for primaries and fragments. (To the extent this is achieved, the resulting ΔE and charge distributions are not biased by the event selection.)

Given these uncertainties, it appears the best method of determining the systematic errors is to compare δD results for data taken with identical targets but at different times. (In the results presented below, when multiple measurements are available, the average is shown.) Several such cases are available for study. For instance, data were taken with the 1.94 g cm-2 CH2 target in four separate runs, with three different configurations of the detectors on the beamline. The four δD_n values obtained average 0.0497 $(g\ cm^{-2})^{-1}$, with a standard deviation of 0.0018, or about 3.6% of the mean. Considering all such cases, we find the quantity (standard deviation)/mean is, for 5 of 6 cases, less than 0.041. The single exception is for the 2 g cm^{-2} carbon target data, which have a greater scatter and give a ratio of 0.10. Accordingly, when multiple measurements for a particular target are

available, we estimate the error to be the larger of the actual standard deviation, or ± 5% of the average value. When only a single depth of a material was used, we take the error to be ± 5% of the measured value.

4. Results

a. Bragg Curves and Dose Reductions

Table 1 lists the elemental target materials and depths tested; Table 2 lists the composite targets studied, many of which were supplied by colleagues at the NASA Langley Research Center, and others by Dr. Raj Kaul at NASA Marshall Spaceflight Center (MSFC). For most composites, we have only a single measurement. In both tables, the measured fractional reduction in dose as measured by the average ΔE method is divided by the target depth to obtain δD_n for each target.

For polyethylene, carbon, aluminum, copper, and lead targets, we show three sets of curves in Figures 3 through 5. All three plots are functions of depth: $\Delta E_{avg\text{-}in}/\Delta E_{avg\text{-}out}$ (Fig. 3), δD (Fig. 4), and δD_n (Fig. 5). Though all three plots contain essentially the same information; each highlights a different aspect of the results.

In Fig. 3, which also includes the three available data points for lucite (polymethylmethacrylate, or PMMA), the curves are essentially Bragg curves. It is readily apparent that the polyethylene curve falls farther and faster than the others. The polyethylene curve is very similar to that obtained for water with the same beam (see Figure 2 of Ref. 7). The limited data for lucite are similar to those for polyethylene, which is to be expected given the similar compositions.

The lack of carbon data at depths above 5 g cm^{-2} is unfortunate, but it seems clear that the data points would fall somewhere between those for polyethylene and aluminum. A calculation using our Monte Carlo model [13] to simulate greater depths of carbon is shown as the dashed line in Fig. 3; it agrees reasonably well with the carbon data points

below 5 g cm^{-2}, and it falls close to the polyethylene curve. It is important to note, though, that the model produces only one fragment per nuclear interaction, which is unrealistic and causes the model to underestimate the measured ΔE's, so that in reality carbon data would almost certainly lie slightly above than the calculated curve shown in the figure. As target mass number increases, the data points fall closer to 1.0 (i.e., small reductions in dose), and the curves get flatter. Aluminum, used extensively in the construction of previous generations of spacecraft, including the Space Shuttle and International Space Station, shows a moderately steep slope out to 16.2 g cm^{-2}, but with little change between that point and the one at 26 g cm^{-2}. Lead shows little change in dose at any depth.

In Fig. 4, the dose reduction is shown as a function of depth. This is slightly different way to look at the same data as in Fig. 3, since $\delta D = 1 - \Delta E_{avg\text{-}in}/\Delta E_{avg\text{-}out}$, but in this representation the differences in slopes between low-A and high-A targets is particularly clear. Finally, in Fig. 5, we plot normalized dose reduction as a function of depth. The data points for all materials are well fit by exponentials of the form $y = ae^{-bx}$. In this context, the fitted values of *a* represent the normalized dose reduction per unit mass at zero, or infinitesimal, depths. This is therefore a useful quantity to compare between materials, and for cases in which at least two depths of a given material were measured, the fit parameters are shown in the far-right columns of Tables 1 and 2. The largest values of *a* are found for polyethylene, lucite, and beryllium, and the other values clearly decrease with increasing target mass number. The slopes, *b*, are about 0.029 (g cm^{-2})$^{-1}$ for CH_2 and lucite, about 0.025 (g cm^{-2})$^{-1}$ for the light elemental targets, and decrease – meaning the fit curves get flatter – as the target mass number increases.

c. Compound Targets

The last two rows of Table 2 show results for two measurements where the target consisted of polyethylene placed behind 5.26 g cm^{-2} of aluminum. Since we have data for these two materials separately, we can check whether the results for the compound targets can be predicted, at least approximately, from the individual components. The first compound target, Al followed by 1.94 g cm^{-2} CH_2, gave a δD_n of 0.026 (g cm^{-2})$^{-1}$; using

the exponential fit values for these depths (Al at 5.26 g cm^{-2} and CH_2 at the full combined depth of 7.2 g cm^{-2}), and adding the two together weighted by the mass fractions, yields a value of $\delta D_n = 0.026$, in excellent agreement with the measurement. Applying this method to the second compound target (4.76 g cm^{-2} CH_2 behind the Al) yields a predicted δD_n of 0.029, also in excellent agreement with the measured value.

The simple ansatz for how the separate properties of the two materials should combine thus leads to predictions that agree well with the data, at least in these two cases. Assuming the method is valid and more generally applicable, one consequence is that the order of the materials on the beamline matters – if the order of the Al and CH_2 were reversed, we would have calculated a slightly larger value for δD_n, 0.030, in the second case. This is a small effect for such modest target depths, but could be significant when greater depths are considered.

d. Results for Hydrogen Target, Comparison to HZETRN

The Al + CH_2 examples above suggest that it is valid to use the results for CH_2 and C to extract a value of δD_n for hydrogen. From Table 1, at zero depth we have for CH_2 and C, respectively, δD_n values of 0.0523 ± 0.0026 $(g\ cm^{-2})^{-1}$ and 0.0386 ± 0.0019 $(g\ cm^{-2})^{-1}$. The weight fractions in CH_2 are 6/7 and 1/7 for C and H, respectively; this leads us to predict that $\delta D_n(H) = 0.123 \pm 0.021$ $(g\ cm^{-2})^{-1}$ at zero depth. This is an impressively large number; it suggests that pure hydrogen would be more than twice as effective as polyethylene in reducing dose, at least in this particular beam. The result is qualitatively consistent with Ref. [5], in which HZETRN was used to calculate the GCR dose equivalent at depth, H(x), divided by unshielded GCR dose equivalent, H(0). This ratio is plotted as a function of depth for pure hydrogen, methane (CH_4), and other compounds. At depths of 1 and 2 g cm^{-2}, hydrogen was predicted to produce H(x)/H(0) of about 0.8 and 0.6, and CH_4 produced values of about 0.91 and 0.82. Defining, in analogy with δD_n, $\delta H_n = (1 - H(x)/H(0))/x$, we obtain 0.09 $(g\ cm^{-2})^{-1}$ for CH_4 and 0.2 $(g\ cm^{-2})^{-1}$ for H; so, in the calculation as well as the data, hydrogen appears to be superior by more than a factor of two when compared to a simple hydrocarbon. (We note that CH_4 is expected to be a more effective shield than CH_2 owing to the higher H fraction.)

The δH_n value for the calculated pure hydrogen target is much larger than the δD_n value we report (0.2 vs. 0.123 g^{-1} cm^2). There are at least two major differences between the data and the calculation. First, we expect part of the difference is due to dose equivalent H(x) being more sensitive to the effect of nuclear fragmentation effects than D(x) is. This is because H(x) is the product of D(x) and the average quality factor, $Q_{av}(x)$. If both D(x) and $Q_{av}(x)$ are decreasing with x, then H(x) will decrease faster than D(x). Second, the δH calculation is for the entire GCR, including many ions at energies well above 1 GeV/nuc; at such high energies, we expect Bragg curves to fall more steeply over the first several g cm^{-2} than do the 1 GeV/nuc curves. The reason for this is related to the shape of the dE/dx curve as a function of projectile energy (or velocity). Particles at or below 1 GeV/nuc fall in the portion of the curve where dE/dx (or LET) is approximately proportional to $1/\beta^2$ where $\beta = v/c$ (i.e., β is the particle's velocity divided by the speed of light). Slowing of primaries and secondaries in the target material increases their LET and thus partially compensates for the effect of fragmentation[5]. At higher energies, above about 3 GeV/nuc, the dE/dx vs. energy curve becomes quite flat, and in fact rises slightly. Thus at these higher energies, there is no significant change in LET as a particle traverses a target, and thus there is no compensation of the decrease in LET caused by fragmentation.

e. Composite Targets

In Table 2, it can be seen that almost all composite targets were available only in a single depth, the exception being graphite-epoxy, which was measured at both 5 and 10 g cm^{-2}. Since the composite targets are all low-A, it is reasonable to assume that δD_n vs. depth curves for these materials would be similar to those found for polyethylene and lucite, i.e., $\delta D_n(x) = ae^{-bx}$ with b close to 0.03. For measurements at 5 g cm^{-2} depth, this implies that $a \approx 1.16\ \delta D_n(5)$, with smaller corrections for the epoxy and boron-epoxy targets. Therefore in Table 2 we show estimated values of a that we would expect to measure if we had used multiple depths of these materials. The estimated a values for the LaRC

[5] With a 600 MeV/nuc ^{56}Fe beam and CH_2 targets, we found that the LET increases due to dE/dx in the target almost exactly compensated for fragmentation, producing a very flat Bragg curve over the first 8 g cm^{-2}. See Ref. [X] for details.

targets (rows starting with graphite epoxy and ending with PETI-5) are all clustered between 0.036 and 0.045 g^{-1} cm^2, with the boron-loaded CH_2 giving the greatest dose reduction and the "Mars Bar" giving the least. It is perhaps not surprising that the Mars Bar, described in detail in [14], is the least effective shield of the group, since it consists of higher-A materials in the form of Martian regolith simulant mixed with polyethylene. The regolith simulant contains O, Si, Fe, Mg, and Ca. It is reasonable to assume from basic nuclear physics considerations that O would be about as effective as C, and that the Si and Mg components would be about as effective as Al. These three elements account for over 90% of the molar weight, in a ratio of about 2:1 (O to Si and Mg combined). Using the values in Table 1, and ignoring the Fe and Ca components, we would predict δD_n = 0.033 g^{-1} cm^2 for the other components. The Fe and Ca contributions would decrease δD_n, while the CH_2 blended into the mixture would increase it. This hand-waving treatment gives reasonable agreement with the measured value of 0.036 g^{-1} cm^2.

The targets supplied by MSFC are of unknown composition and are labeled according to the information supplied. There is relatively little variation in shielding performance among the four materials tested; all give a_{est} values in the range 0.043 to 0.048 g^{-1} cm^2. These materials, developed much more recently than the NASA LaRC targets, are only slightly less effective than polyethylene.

f. Rankings

In Fig. 6, we display the results for the parameter a, in units of $(g\ cm^{-2})^{-1}$, as a bar graph. For the target materials where two or more data points were obtained, the value shown is the result of an exponential fit to δD_n vs. depth. For those where only a single measured point was available, the plotted values are the a_{est} numbers shown in Table 2, i.e., the measured values adjusted upwards by 3 to 16% depending on target depth.

Figure 6 allows us to draw several conclusions. First, to the extent that the 1 GeV/nuc ^{56}Fe beam stands as a proxy for the heavy-ion component of the GCR, we have experimental confirmation of the predictions of Wilson et al. in Ref. 9. It is abundantly clear that shielding effectiveness decreases as the mass number of the material increases,

and that a pure hydrogen shield would be optimal. Beryllium also appears to be a highly effective shield, but is a problematic material for other reasons. Second, we note the rather narrow range of performance found over a variety of composites, so that a decision about which of them to choose for shield construction can be based on other material properties that are important for human spaceflight – e.g., structural performance, longevity in the deep-space environment, lack of outgassing, etc. Third, we note the possible significance of the ordering of materials in a compound (layered) shield; the data suggest that there is an advantage in using a lower-A material as the skin, or perhaps a layer just below the skin, of the spacecraft. Lower-A materials are advantageous for neutrons, as well, because of the reduction in target-evaporation neutrons [15], which are predominately low energy (< 20 MeV) neutrons with high biological weighting factors.

In Fig. 7, we show for the elemental targets measured, the fit parameter *a* vs. mass number. The data are reasonably well fit by an inverse second-order polynomial; the fit parameters are shown in the plot. This may provide a simple but useful tool for estimating dose reduction for thin layers of elemental materials for which no data are presently available.

5. Conclusions

Beams of 1 GeV/nuc ^{56}Fe provided by the Brookhaven National Laboratory's AGS and NSRL accelerators have been used to measure shielding properties of several elemental and composite target materials. Although a single experiment cannot replicate the complexity of the full GCR spectrum, some of the important characteristics of the heavy-ion component of the GCR are represented by this beam. At the fairly modest target depths considered here, the dose and dose equivalent behind even the thickest targets are dominated by charged particles, and no attempt has been made to measure or otherwise include contributions from neutrons. The experimental data obtained have been presented as Bragg curves where possible, and as both total dose reduction and dose reduction per unit mass. Plots of dose reduction per unit mass vs. depth are reasonably well-fit by

simple exponentials; the first coefficient of each fit corresponds to the dose reduction per unit mass at infinitesimal depths, providing a common basis for comparing materials.

The results of the analysis accord well with the conclusions of Wilson et al.: hydrogen is by far the most effective shielding material. (Measurements using a helium target would also be of interest if such a target could be procured.) Shields with higher mass numbers have less effectiveness per unit mass at shallow depths and show relatively little change per unit mass as depth increases. As shown by their larger slopes in the exponential fits, lighter materials become less effective per unit mass as depth increases, but still retain a considerable advantage over the higher-A materials, even at the greatest depths considered here. Composite targets provided by materials scientists at the NASA Langley Research Center were all less effective than CH_2, and all showed similar performance as shields, with δD_n varying within about ± 10% of the average for the group. More recently-developed materials from NASA MSFC were slightly better than the LaRC targets, but still not as effective as polyethylene.

6. Acknowledgments

We thank the operators and staff of the AGS accelerator at Brookhaven National Laboratory for their considerable efforts to produce the iron beam for these experiments. Our requirements are substantially different from those of other users on the same beamline, and we appreciate the extra work required to produce the low intensity and long spill that are needed for our equipment to operate efficiently and without damage to the silicon detectors. In particular we thank our liaison physicist, Dr. Donald Lazarus, for his efforts on our behalf. We also thank Drs. Adam Rusek and I-Hung Chang for their considerable help at both the AGS and NSRL experiments. We are grateful to Dr. Raj Kaul of NASA MSFC, and to Drs. John Wilson and Sheila Thiebault at NASA LaRC, for providing composite targets. We are also particularly grateful to Dr. Wilson for performing the calculations that motivated us to do this analysis. This work was

performed under NASA Contracts numbers L14230C, H31910D and H34854D, through the U.S. Department of Energy under Contract No. DE-AC02-05CH11231.

References

[1] National Council on Radiation Protection and Measurements, Radiation Protection Guidance for Activities in Low-Earth-Orbit, NCRP Report 132, Bethesda, MD, 2000.

[2] Bioastronautics Roadmap: A Risk Reduction Strategy for Human Space Exploration, NASA/SP-2004-6113 (2005), online at http://bioastroroadmap.nasa.gov .

[3] R. A. Mewaldt, A. J. Davis, W. R. Binns, G. A. de Nolfo, J. S. George, M. H. Israel, R. A. Leske, E. C. Stone, M. E. Wiedenbeck, and T. T. von Rosenvinge, The cosmic ray radiation dose in interplanetary space – present day and worst-case evaluations, presented at the 29th International Cosmic Ray Conference, Pune, India.

[4] L. C. Simonsen and J. E. Nealy, Technical Paper 3079, National Aeronautics and Space Administration, 1991.

[5] J. W. Wilson, F. F. Badavi, F. A. Cucinotta, J. L. Shinn, G. D. Badhwar, R. Silberberg, C. H. Tsao, L. W. Townsend, and R. K. Tripathi, HZETRN: Description of a Free-Space Ion and Nucleon Transport and Shielding Computer Program. Technical Paper 3495, National Aeronautics and Space Administration, 1995.

[6] C. Zeitlin, L. Heilbronn, J. Miller, S. E. Rademacher, T. Borak, T. R. Carter, K. A. Frankel, W. Schimmerling and C. E. Stronach, Heavy fragment production cross sections from 1.05 GeV/nucleon 56Fe in C, Al, Cu, Pb, and CH2 targets, Phys. Rev. C, 56, (1997) 388.

[7] C. Zeitlin, L. Heilbronn and J. Miller, Detailed Characterization of the 1087 MeV/nucleon Iron-56 Beam Used for Radiobiology at the Alternating Gradient Synchrotron, Rad. Res. 149, (1998) 560.

[8] S. B. Guetersloh, C. Zeitlin, L. Heilbronn, J. Miller, and T. Komiyama, Analysis of polyethylene radiation shielding in the cosmic-ray environment, submitted to Nuclear Instruments and Methods B (2006).

[9] J. W. Wilson, M. Kim, W. Schimmerling, F. F. Badavi, S. A. Thibeault, F. A. Cucinotta, J. L. Shinn and R. Kiefer, Issues in space radiation protection: galactic cosmic rays. Health Phys. 68, (1995) 50.

[10] L. W. Townsend, J. E. Nealy, J. W. Wilson, and L. C. Simonsen, Estimates of Galactic Cosmic Ray Shielding Requirements During Solar Minimum, Technical Memorandum 4167, National Aeronautics and Space Administration, 1990.

[11] A. S. Goldhaber, Phys. Lett. 53B (1974) 306.

[12] C. Zeitlin, A. Fukumura, L. Heilbronn, Y. Iwata, J. Miller, and T. Murakami, Fragmentation cross sections of 600 MeV/nucleon 20Ne on elemental targets, Phys. Rev. C 64, (2001) 024902.

[13] C. Zeitlin, L. Heilbronn, J. Miller, W. Schimmerling, L.W. Townsend, R.K. Tripathi, J.W. Wilson, Radiat. Res. 145 (1995) 666.

[14] L. Heilbronn, Y. Iwata, H. Iwase, T. Murakami, H. Sato, T. Nakamura, R. M. Ronningen, K. Ieki, I. Gudowska, and N. Sobolevsky, Secondary neutron-production cross sections from heavy-ion interactions in composite targets, Phys. Rev. C 73, 024603 (2006).

[15] F. A. Cucinotta, Caclulations of cosmic-ray helium transport in shielding materials, Technical Paper 3354, National Aeronautics and Space Administration, 1993.

Table 1 – Fractional Dose Reduction Behind Elemental Targets

Material	Depth (g cm^{-2})	δD_n(g^{-1} cm^2)	Fit *a, b*
Beryllium	2.35	0.048	0.0507, 0.0248
	4.69	0.045	
Carbon	0.90	0.038	0.0386, 0.0253
	1.68	0.037	
	2.00	0.036	
	3.68	0.037	
	3.99	0.034	
Aluminum	1.76	0.021	0.0234, 0.0235
	3.51	0.022	
	7.02	0.021	
	11.6	0.020	
	16.2	0.017	
	26.0	0.011	
Copper	2.81	0.012	0.0136, 0.0155
	5.63	0.012	
	5.86	0.014	
	11.3	0.011	
	19.5	0.0096	
Tin	3.66	0.0085	
Lead	3.39	0.0034	0.0040, 0.0112
	6.78	0.0036	
	14.4	0.0045	
	30.0	0.0023	

Table 2 – Fractional Dose Reduction Behind Composite Targets

Material	Depth (g cm^{-2})	δD_n(g^{-1} cm^2)	Fit *a, b*
Polyethylene	1.94	0.050	0.0507, 0.0289
	3.28	0.045	
	3.6	0.048	
	3.76	0.045	
	4.76	0.044	
	5.0	0.041	
	6.3	0.042	
	9.4	0.039	
	13.1	0.035	
	13.5	0.034	
	17.0	0.032	
Lucite	1.28	0.047	0.0504, 0.0291
	2.55	0.048	
	22	0.026	
Graphite Epoxy	5.0	0.035	0.0377, 0.0148
	10.0	0.033	
Boron Epoxy	1.0	0.040	a_{est} = 0.041
Pure Epoxy	1.31	0.041	a_{est} = 0.043
CH_2 + B	5.0	0.039	a_{est} = 0.045
Martian Regolith + CH_2 (“Mars Bar”)	5.0	0.031	a_{est} = 0.036
Polyethylene + LiC	5.0	0.037	a_{est} = 0.043
LiF	5.0	0.038	a_{est} = 0.043
CH_2 + ^{6}Li	5.0	0.038	a_{est} = 0.044
PETI-5	5.0	0.033	a_{est} = 0.038
MSFC 645	4.63	0.043	a_{est} = 0.049
MSFC FC1	4.4	0.041	a_{est} = 0.047
MSFC G3C11	3.28	0.041	a_{est} = 0.045
MSFC 824	3.76	0.043	a_{est} = 0.048
Al (5.26 g cm^{-2}) + CH_2 (1.94 g cm^{-2})	7.2	0.026	
Al (5.26 g cm^{-2}) + CH_2 (4.76 g cm^{-2})	10.0	0.028	

Figure Captions

Figure 1. Typical charge spectra as seen in large- and small-acceptance detectors. All fragment peaks can be resolved at small acceptance, however the differences between the dose reductions measured at large and small acceptance are on the order of 10% or less.

Figure 2. Scatter plot of normalized dose reduction determined by the two different analysis methods, for a subset of the data . See the text for details.

Figure 3. Measured event-averaged ΔE, divided by target-out ΔE, as a function of depth for different target materials. A Monte Carlo calculation for carbon targets of depth greater than 5 g cm^{-2} is also shown as the heavy dashed line; the calculation underestimates the number of fragments emerging from the target, so that actual data points would lie slightly above the line.

Figure 4. Dose reduction as a function of depth for elemental targets and polyethylene.

Figure 5. Dose reduction as per Fig. 4, divided by target depth. The curves are fits of a simple exponential form to the data; fit parameters are given in Tables 1 and 2. The error bars correspond to the ± 5% systematic uncertainty described in the text.

Figure 6. Normalized dose reduction ranked from highest to lowest. The relative uncertainty for the hydrogen measurement is larger than for other materials due to the propagation of errors in both C and CH_2 data.

Figure 7. Dose reduction per g cm^{-2} as given by the fit parameter *a*, as a function of target mass number, shown with a fit to an inverse second-order polynomial.

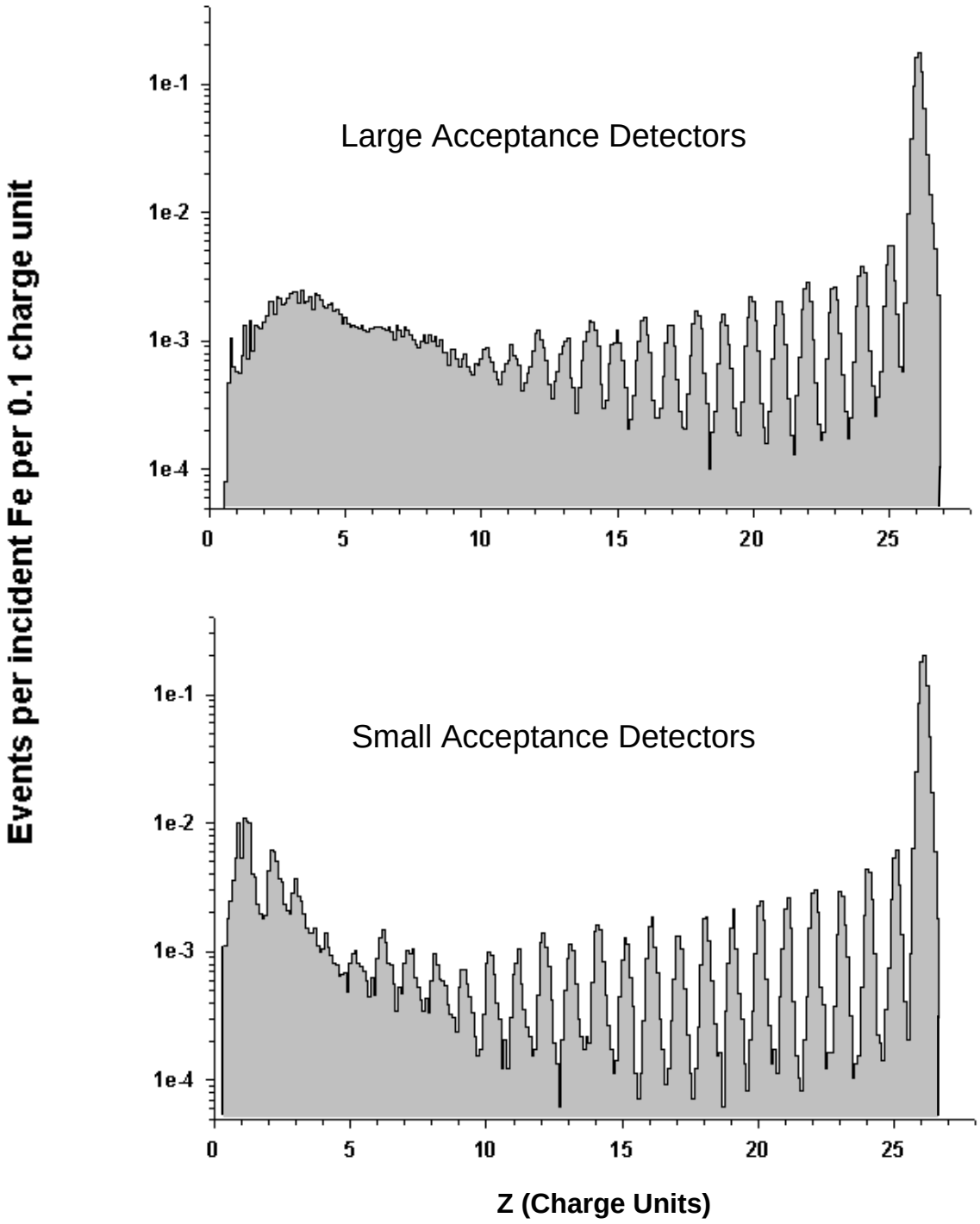
Large Acceptance Detectors
Small Acceptance Detectors
Events per incident Fe per 0.1 charge unit
1e-1
1e-2
1e-3
1e-4
0
5
10
15
20
25
Z (Charge Units)

FIGURE 1

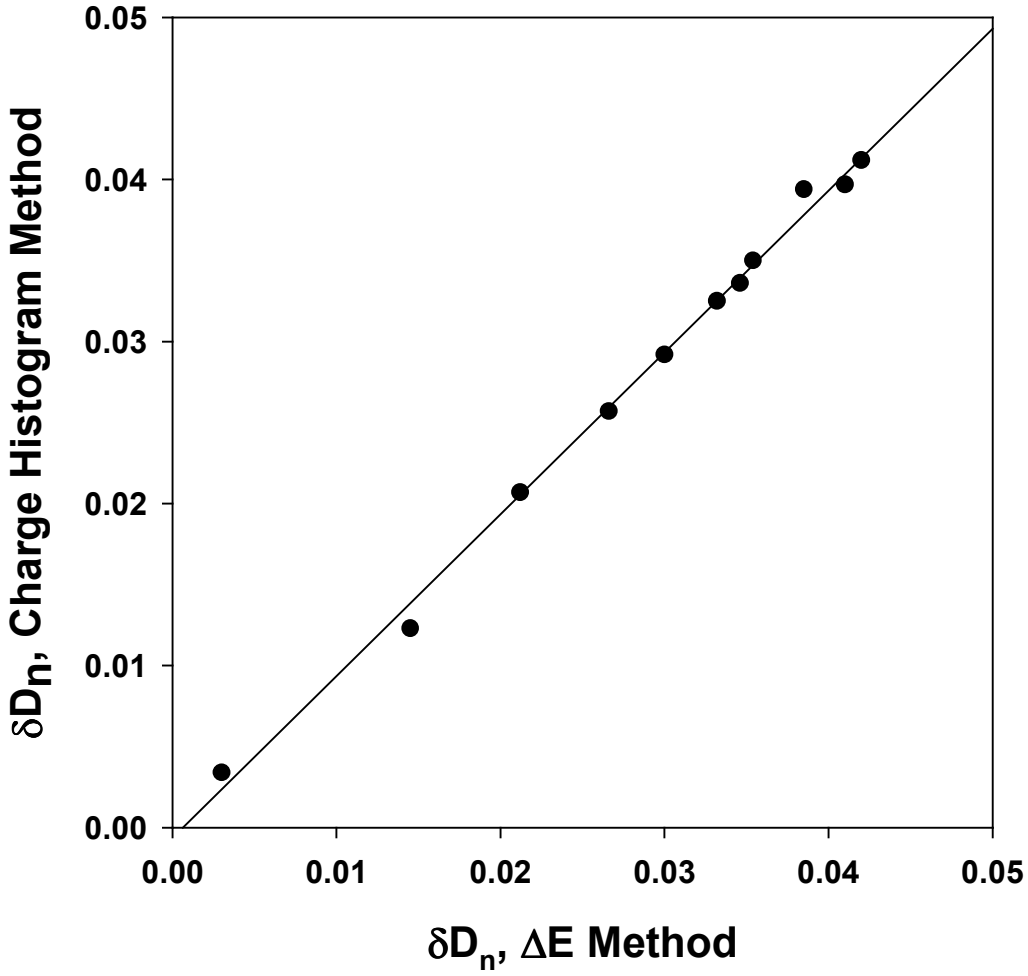
0.05
0.04
0.03
0.02
0.01
0.00
0.00
0.01
0.02
0.03
0.04
0.05
δDn, Charge Histogram Method
δDn, ΔE Method

FIGURE 2

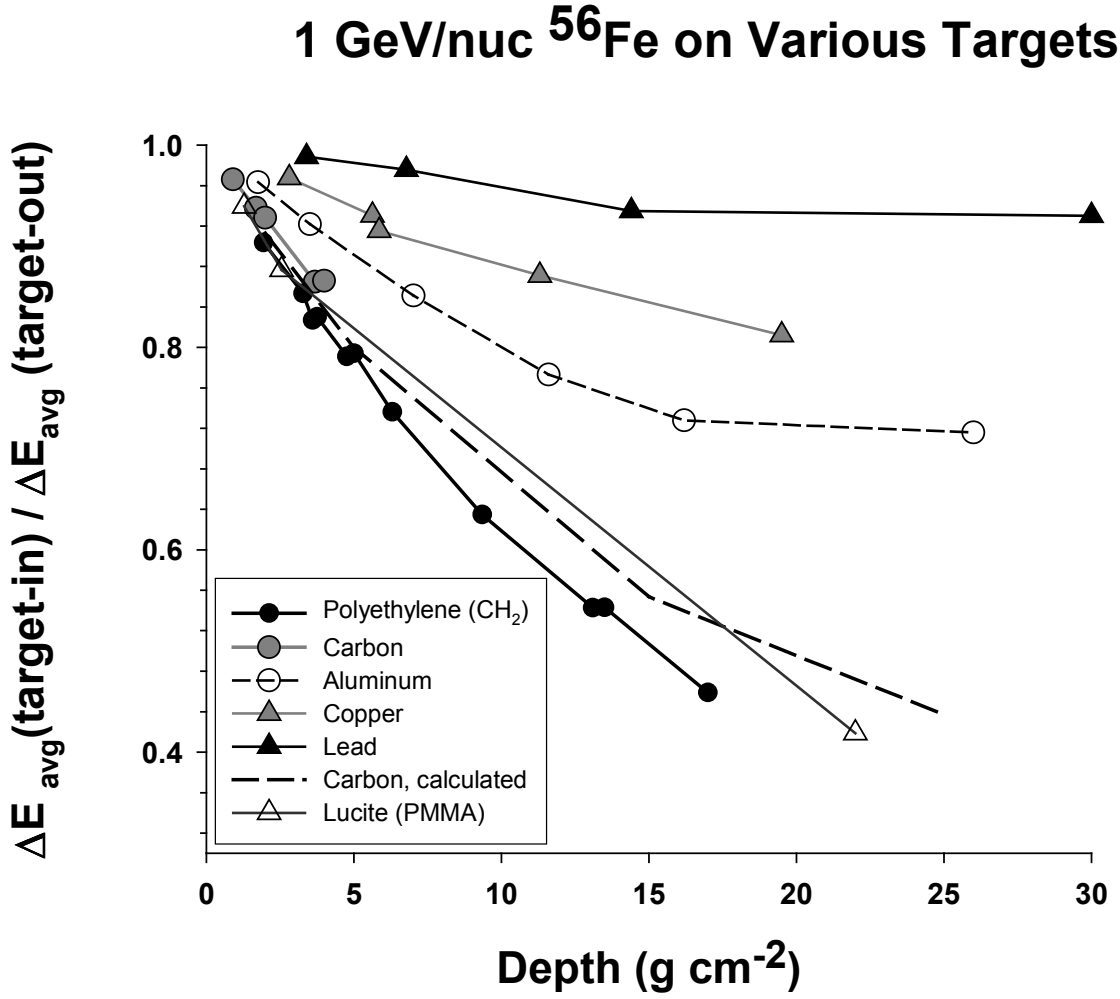
1 GeV/nuc 56Fe on Various Targets
ΔE avg(target-in) / ΔEavg (target-out)
1.0
0.8
0.6
0.4
0
5
10
15
20
25
30
Depth (g cm-2)
Polyethylene (CH2)
Carbon
Aluminum
Copper
Lead
Carbon, calculated
Lucite (PMMA)

FIGURE 3

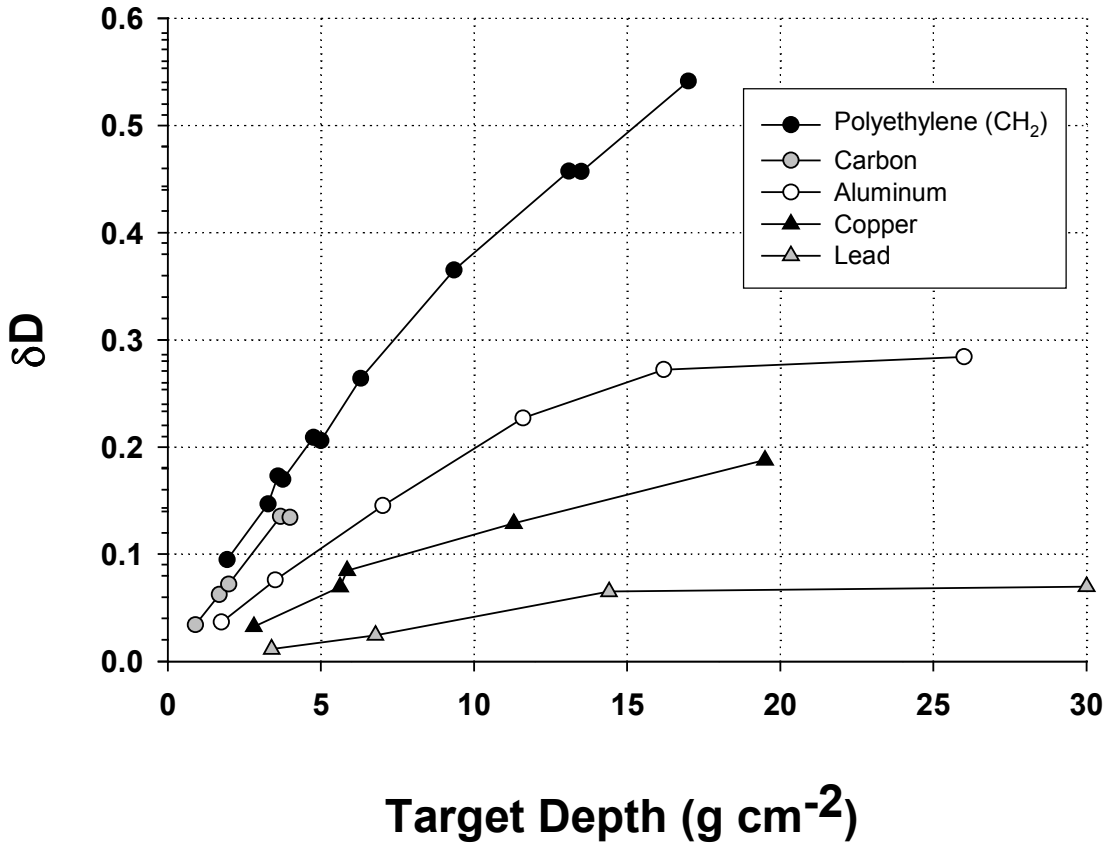
0.6
0.5
0.4
0.3
0.2
0.1
0.0
δD
0
5
10
15
20
25
30
Target Depth (g cm-2)
Polyethylene (CH2)
Carbon
Aluminum
Copper
Lead

FIGURE 4

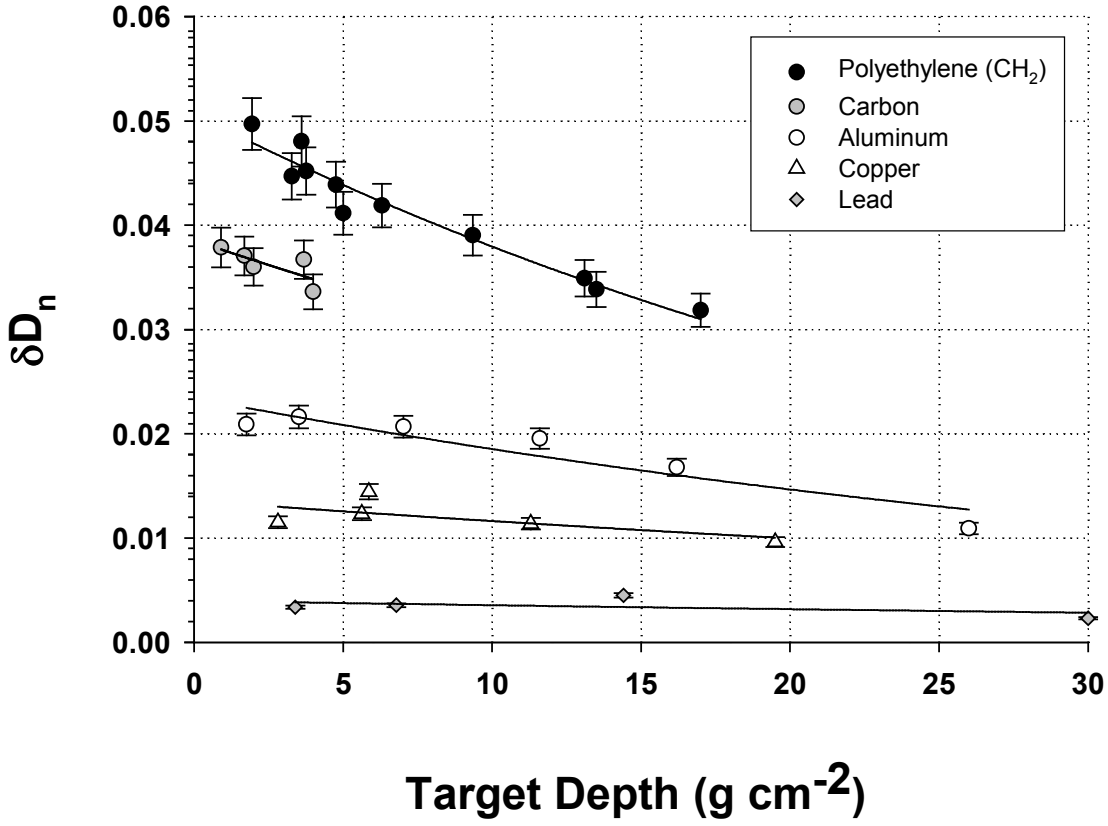
0.06
0.05
0.04
0.03
0.02
0.01
0.00
δD_n
0
5
10
15
20
25
30
Target Depth (g cm^-2)
Polyethylene (CH2)
Carbon
Aluminum
Copper
Lead

FIGURE 5

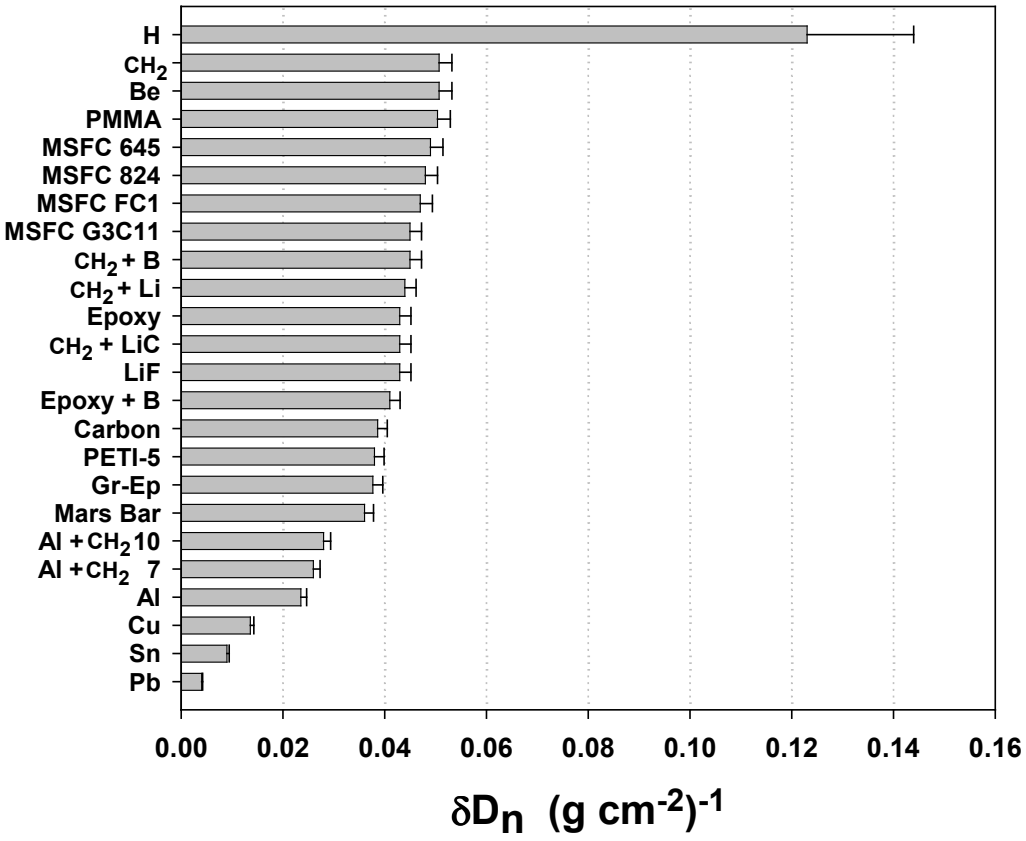
H
CH2
Be
PMMA
MSFC 645
MSFC 824
MSFC FC1
MSFC G3C11
CH2 + B
CH2 + Li
Epoxy
CH2 + LiC
LiF
Epoxy + B
Carbon
PETI-5
Gr-Ep
Mars Bar
Al + CH2 10
Al + CH2 7
Al
Cu
Sn
Pb
0.00
0.02
0.04
0.06
0.08
0.10
0.12
0.14
0.16
δDn (g cm-2)-1

FIGURE 6

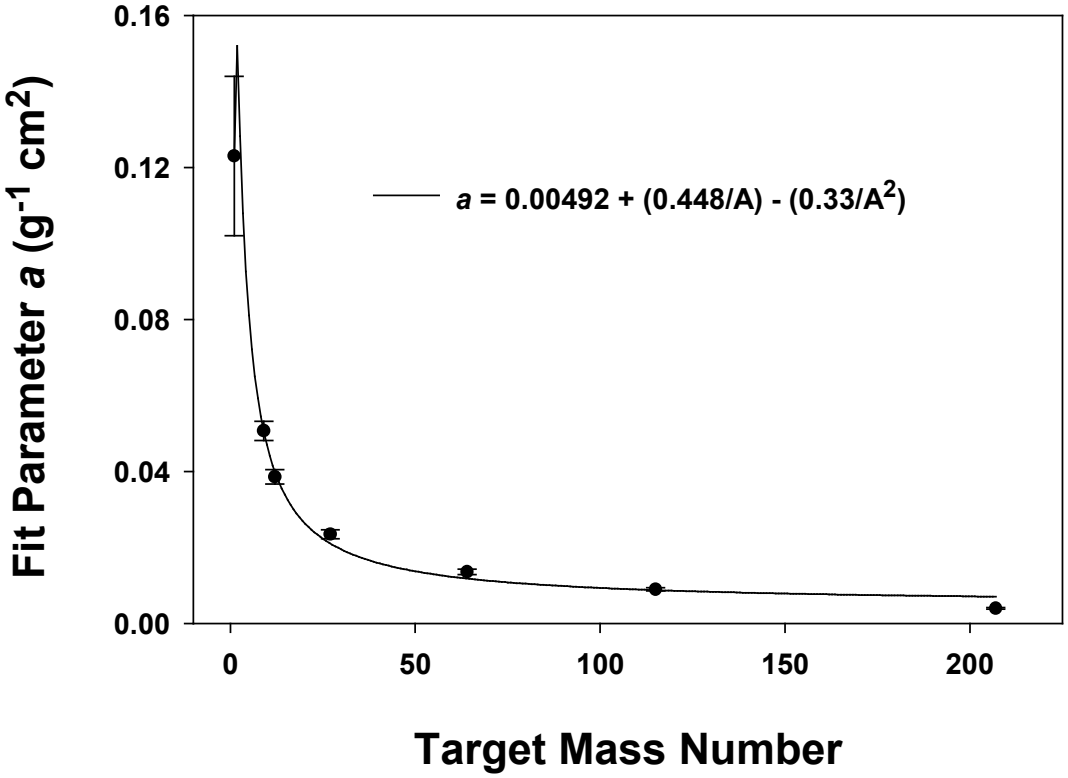
0.16
0.12
0.08
0.04
0.00
0
50
100
150
200
Fit Parameter a (g-1 cm2)
Target Mass Number
a = 0.00492 + (0.448/A) - (0.33/A2)

FIGURE 7